A Robot Application for Marine Vessel Inspection

Markus Eich
DFKI - Robotics Innovation Center
28359 Bremen, Germany
markus.eich@dfki.de

Francisco Bonnin, **Emilio Garcia** and **Alberto Ortiz**
University of the Balearic Islands
07122 Palma de Mallorca, Spain
alberto.ortiz@uib.es

Gabriele Bruzzone
ISSIA - CNR (Via De Marini 6)
16149 Genoa, Italy
gabriele.bruzzone
@ge.issia.cnr.it

Yannis Koveos
Glafcos Marine Ltd.
18537 Piraeus, Greece
ykovaios@glafcos-marine.com

Frank Kirchner
DFKI - Robotics Innovation Center
28359 Bremen, Germany
frank.kirchner@dfki.de

Abstract

Seagoing vessels have to undergo regular inspections, which are currently performed manually by ship surveyors. The main cost factor in a ship inspection is to provide access to the different areas of the ship, since the surveyor has to be close to the inspected parts, usually within hand's reach, either to perform a visual analysis or to take thickness measurements. The access to the structural elements in cargo holds, e.g., bulkheads, is normally provided by staging or by 'cherry-picking' cranes. To make ship inspections safer and more cost-efficient, we have introduced new inspection methods, tools, and systems, which have been evaluated in field trials, particularly focusing on cargo holds. More precisely, two *magnetic climbing robots* and a *micro-aerial vehicle*, which are able to assist the surveyor during the inspection, are introduced. Since localization of inspection data is mandatory for the surveyor, we also introduce an external *localization system* which has been verified in field trials, using a climbing inspection robot. Furthermore, the inspection data collected by the robotic systems is organized and handled by a *spatial content management system* which permits comparing the inspection data of one survey with that from another, as well as documenting the ship inspection when the robot team is used. *Image-based defect detection* is addressed by proposing an integrated solution for detecting corrosion and cracks. The systems' performance is reported, as well as conclusions on their usability, all in accordance with the output of field trials performed onboard two different vessels under real inspection conditions.

1 Introduction

For obvious reasons, large tonnage vessels, such as bulk carriers, dry cargo ships, or tankers (see Fig. 1), undergo regular inspections to prevent structural damage that can compromise the vessel's integrity. These inspections are usually performed in accordance with an inspection programme that depends on the requirements of the so-called *classification societies* (in short, *the classes*), and comprise visual close-up surveys as well as thickness measurements obtained by means of non-destructive testing methods (NDT) (Tanneberger and Grasso, 2011). For a close-up survey, the surveyor has to get within hand's reach of the part under observation for adequate visual inspection. Structural damage, pitting, and corrosion are visually estimated based on the experience of the surveyor, and the inspection process is usually documented, using cameras to take images, chalk and pen for defect marking, and a clipboard for note taking. Some solutions based on unmanned underwater vehicles (UUV) have been proposed lately for the inspection of underwater areas, e.g., the hybrid ROV solution by ECA Robotics (http://www.eca-robotics.com), the

Figure 1: Illustration of traditional inspection methods: (left) general cargo ship, (center) staging previous to inspection, and (right) cherry-picking. [Source: (left,center) Lloyd's Register, (right) http://www.standard-club.com]

HAUV by Bluefin (Kaess et al., 2010), and the VideoRay ROVs (http://www.videoray.com/). The first two systems are primarily intended for underwater hull survey while the latter is for water tank inspection.

Regarding the inspection of dry areas, providing access to the relevant parts of the ship, e.g. inside the cargo hold of a bulk carrier, is the most time-consuming part of the inspection process. As can be seen in Fig. 1(center), traditional ship surveying methods comprise, prior to the survey, the installation of scaffolding to allow the surveyor to inspect structures such as bulkheads, beams, stiffeners and brackets, which are usually several meters above the bottom of the hold. Besides the scaffolding, "cherry-picking" methods are also employed: in this case, the surveyor reaches the point of interest inside a basket, transported by a tower crane or by a hydraulic arm (Fig. 1(right)). Clearly, these procedures can be dangerous for the surveyor. For this reason, and because of the high costs of gaining access to a ship for inspection, the EU-funded research project MINOAS (Caccia et al., 2010b) set up a consortium to introduce robots into the ship surveying process. The basis of the consortium's expertise comprised two classification societies, different marine service providers, and partners involved in robotics research. The key idea was to introduce a set of novel tools to enhance the ship surveying process. For the interested reader, a more detailed discussion of the application scenario can be found in (Ortiz et al., 2010).

This paper reports results of the introduction of heterogeneous robots to the area of close-up surveys of the structural elements of large-tonnage vessels, where most of the work is still performed manually. The effort is a mixture of novelty and integration, and the proportion of each is different for every platform. Nevertheless, the main contribution is the fully integrated inspection system, covering all the stages of an inspection procedure based on the use of robots and supporting software, something that did not exist before the project MINOAS. We introduce a heterogeneous robot team with different locomotion abilities, namely a micro-aerial vehicle (MAV), a lightweight magnetic crawler supported by an external positioning unit, and a heavyweight magnetic crawler equipped with a manipulator arm for thickness measurement. Two additional systems were developed to assist the surveyor: a spatial content management system (SCMS) to host and present in a centralized way the inspection data collected by all the platforms, and a visual defect detection solution for automatic defect detection. They are all described in the following sections.

2 Re-Engineered Inspection Procedure

On the basis of the expertise of the classes involved and the maritime industry, and as part of the MINOAS project working plan, a total of three stages were defined in order to implement an inspection procedure based on robots and compatible with the requirements of the classes (Tanneberger and Grasso, 2011).

Stage 1: *Fast visual inspection overview*. The goal of this stage is to cover large areas of selected parts of the inner hull, supplying visual inspection data to get a rough overview about the state of the vessel, and searching for defects, such as coating breakdown, corrosion and cracks. The images collected must be tagged with pose information since the areas of interest for Stages 2 and 3 are visually selected in this phase. Due to the aforementioned, an aerial platform turns out to be the best option. In more detail, the vehicle must be able to perform vertical, stationary and low speed flight in indoor environments.

Stage 2: *Visual close-up survey*. The procedure in Stage 2 is to get a better impression of the coating and the possible damages, and mark the defective areas in order to repair the damage or perform thickness measurements. The vehicle must be capable of moving on horizontal, sloped, and vertical ferromagnetic surfaces. At this stage, the camera of the robot has to be steady and very close to the structural parts in order to provide high resolution, high quality images. Proper lighting of the area under inspection should be provided. Marking the defects directly on the structure, once confirmed by the surveyor, would be an optional feature of the robot. The acquired images have to be tagged with positioning information. Finally, ease of system setup is also required. Under these constraints, a lightweight, magnetic crawler was considered to be a suitable platform.

Stage 3: *Thickness measurement collection*. At selected parts identified during Stage 2, the thickness of the material is determined by taking measurements at selected points of the hull. The locomotion speed is not important, and the setup requirements are permitted to be more onerous than for Stages 1 and 2. The main goal of Stage 3 is to collect thickness measurements at selected points of the hull structures. Motion over horizontal, sloped and vertical ferromagnetic surfaces is still required. Compared to Stage 2, a higher payload capability is required in order to transport thickness measurement devices and a suitable manipulator arm. The climbing robot has to be able to move inside shell frames of the type shown in Fig. 2. Constraints on the vehicle size are imposed by the need of maneuvering between the T-shaped shell frames of the size indicated in Fig. 2(right). A heavyweight inspection system was selected to fulfill the requirements for this stage.

Table 1 specifies the relation between the different systems and the mission stage where they are used.

Table 1: Relation between systems and inspection stages

System	**Stage 1**	**Stage 2**	**Stage 3**
Aerial platform	×		
Lighweight inspection system (crawler & localization device)		×	
Heavyweight inspection system (crawler & NDT thickness measurement device)			×
Defect detection system	×	×	
Spatial contents management system	×	×	×

The MINOAS inspection procedure places suitable robots into the inspection process, but is generic enough to cover all the requirements of a traditional close-up survey, and becomes therefore the basis for a fully robot-based inspection procedure for marine vessels. Nevertheless, since a very significant fraction of the inspection effort at the structural level (as specified by the rules set for the classes) is spent on cargo holds and on the different elements they involve, e.g., bulkheads, stiffeners, and cross-decks, the developments and tests in this paper refer mostly to cargo holds.

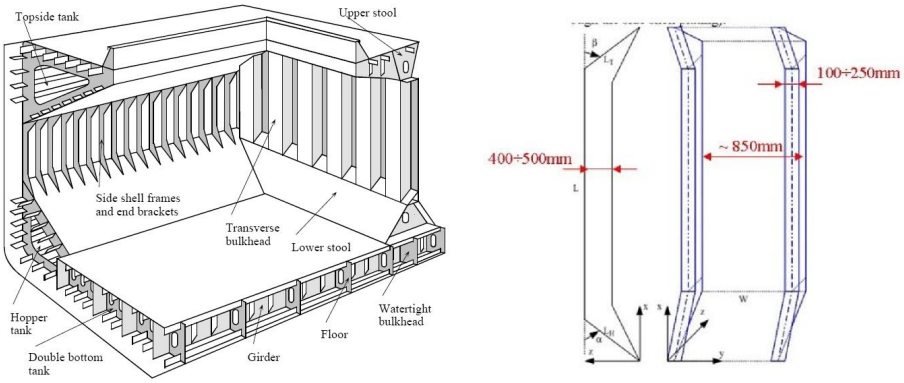

Figure 2: (left) Bulk carrier hold. (right) Shape and size of a shell frame.

3 MINOAS Inspection Platforms

3.1 Related Work on Inspection Platforms

This section reviews previous work that could match the requirements for the MINOAS platforms. Due to their different natures, aerial platforms and crawling systems are considered separately, the latter referring jointly to both the lightweight and the heavyweight inspection systems.

3.1.1 Aerial platforms

MAVs have increased their popularity as robotic platforms in recent years. Their development has been driven by commercial, research, government, and military purposes. This kind of vehicle allows accessing hazardous environments, usually difficult to reach by humans or ground vehicles. These robots are an adequate solution for inspection tasks at, e.g., remote or safety-compromised areas. In order for these platforms to achieve autonomy, a full navigation solution is required. Lately, a number of navigation solutions have been proposed for multi-rotors, including platform stabilization, self-localization, mapping, and obstacle avoidance. They mainly differ in the sensors used to solve these tasks, the amount of processing that is performed onboard/off-board, and the assumptions made about the environment. The laser scanner has been extensively used due to its accuracy and speed. For instance, (Dryanovski et al., 2013; Grzonka et al., 2012) propose full navigation systems using laser scan matching and IMU fusion for motion estimation embedded within SLAM frameworks that enable such MAVs to operate indoors. In (Bachrach et al., 2011; Dryanovski et al., 2013) a multi-level approach is described for 3D mapping tasks. Infrared or ultrasound sensors are other possibilities for implementing navigation solutions. Although they typically have less accuracy and require higher noise tolerance, several researchers (Bouabdallah et al., 2005; Matsue et al., 2005; Roberts et al., 2007) have used them to perform navigation tasks in indoor environments, since they are a cheaper option than laser scanners. Vision based navigation has become quite popular for MAVs lately. Cameras' success in general robotics comes mainly from the richness of the sensor data supplied, combined with their low weight, low power designs, and relatively low prices. Nevertheless, for the particular case of MAVs, the associated higher computational cost has made researchers find optimized solutions that can run over low-power processors. Among the most recent papers published in this regard, some propose visual SLAM solutions based on feature tracking, either adopting a frontal mono or stereo camera configuration, e.g. (Fraundorfer et al., 2012), or choosing a ground-looking orientation, e.g. (Chowdhary et al., 2013). Others focus on efficient implementations of optical flow calculations, either dense or sparse, and mostly from ground-looking cameras, e.g. (Zingg et al., 2010), or develop methods for landing, tracking and taking off using passive, e.g. (Meier et al., 2012), or active markers, e.g. (Wenzel et al., 2011), also using a ground-looking camera.

3.1.2 Climbing robot platforms

The field of wall climbing robots, which naturally turns out to be relevant for this application, has received a certain amount of attention since the late 1990s (Silva and Tenreiro, 2010). Referring specifically to marine applications, a robotic system which was developed to inspect hot welding seams was introduced by (Shang et al., 2008). This small-sized system has a weight of 30 kg, requires a safety-rope during operation, and uses an infrared sensor to check the temperature of the hot seam after welding. Heavyweight hull cleaning robots have also been used for ship surveying and repair. These robots weigh more than 100 kg and are used to remove large areas of coating on the ship's hull using water jetting techniques or brushes (Ortiz et al., 2007). Some robots are already available for marine inspection services, such as the robot Steel-Climber from Miko Marine (Miko, 2013) or the Magnet Crawler M250 from Jetstream Europe (Jetstream, 2013). Both are heavyweight magnetic crawlers for blasting, ship cleaning, and inspection. The robot CROMSKI (Jung et al., 2010) is used for dam inspection and is able to climb vertical walls, independently of the material of the wall. Another robot using a tracked system with suction pads is described in (Kim et al., 2010). The robot is a self-contained system which also integrates the motor that produces the vacuum. Another suction-pad based climbing approach is described in (Raut et al., 2010). It enables the robot to walk on glossy and flat surfaces for window cleaning in buildings, and also relies on clean surfaces. An example of a robot using magnetic wheels for inspection purpose is described in (Tâche et al., 2009). The adaptability of the system is provided by different joints which allow the adjustment of the robot's kinematics. A tracked robot using permanent magnets is described in (Kalra

et al., 2006).

3.2 Aerial Inspection Robot for Stage 1

3.2.1 General overview and design of the robot

The MAV prototype is based on the well-known Pelican quadrotor from Ascending Technologies (see Fig. 3(a)). This is a 50-cm diameter platform with 25.4 cm propellers, able to carry a payload of 650 g, and equipped with a standard navigation sensor suite: a barometric pressure sensor for height estimation, a GPS receiver, and a full 3-axis inertial measuring unit (IMU). Furthermore, the MAV has a Hokuyo lightweight laser scanner with a range of up to 30 m, which is not only used for obstacle detection, but, by deflection of lateral beams using mirrors, to estimate the distance to the floor as well as to the ceiling. Visual information is collected by means of a flexible vision system with an appropriate structure for supporting one ground-looking camera and two additional units, which can be tailored for the particular inspection mission to be performed, such as: two forward-facing cameras forming a stereo vision system, one camera facing forward and the other facing upwards, or, to save weight, a single camera facing forward. Apart from the onboard controllers, the vehicle carries an additional high level processor (HLP) which obviates the need to send sensor data to a base station, since it processes it onboard, thus avoiding any communications latency inside the critical control loops. The configuration shown in Fig. 3(a) includes a CoreExpress board fitted with an Intel Atom 1.6 GHz processor and 1 GB RAM. The different sensors are attached to the HLP through USB. Finally, communications are implemented through a WiFi link. The wireless device attached to the vehicle is connected to the HLP using a dedicated PCI Express port, avoiding the need for wireless communications to share USB bandwidth.

3.2.2 Control architecture

As on similar platforms, the control software architecture comprises at least two physically separated agents: the MAV itself and a ground station. More specifically, the different computational resources of the MAV run the control algorithms as follows (either as firmware or as software): (1) as is well known in the Pelican, the main ARM7 low level controller (LLC) runs the low-level software taking care of attitude stabilization and direct motor control (Gurdan et al., 2007); (2) the secondary ARM7 high level controller (HLC) runs the position controller described in (Achtelik et al., 2011); and (3) the HLP executes, on top of the Robot Operating System (ROS) running over Linux Ubuntu, ROS nodes providing platform motion estimates as well as platform safety, interaction with the onboard platform controllers, and WiFi communication with the ground station. Finally, in our configuration, the ground station comprises a cluster of laptops running ROS/Linux Ubuntu to perform off-board operations.

Figures 3(b–c) depict the control software running on the HLP and on the ground station. It features self-localization, mapping, obstacle avoidance, and path planning modules as well as mission control and supervision modules. Self-localization, as a central capability for this platform, is implemented following a 2D laser-based motion estimation approach (in accordance with the requirements of Stage 1). In more detail, the control software permits operation in both semi-autonomous and autonomous modes. In the first mode of operation, an operator is expected to send velocity commands in x, y and z using the sticks of a remote control (RC) unit, while the vehicle provides hovering and height control functionalities using the onboard sensors and the low-level attitude/position controllers. In the second mode of operation, the vehicle performs autonomously missions described by means of mission specification files (MSF, see Fig. 3(d) for a very simple example). In short, MSFs are parsed in order to identify and perform the actions requested (*go-to*, *navigate-to* and *take-photo*) making use of the sensor data processing components, laser pre-processing, vertical position, and odometry, whose results feed the SLAM and the navigation components, together with the low-level controllers. Finally, a safety manager implements a number of safety behaviors, such as monitoring *go-to* and *navigate-to* actions before sending the corresponding motion commands to the HLC, preventing the robot from flying too high or too close to the ceiling, and monitoring the battery voltage.

Among the different components enumerated above, the ground station runs those control modules that can tolerate latency in the communications, namely simultaneous localization and mapping, path planning, and mission execution/supervision, while critical control loops run onboard the vehicle in order to ensure minimum delay, a requirement

(a)

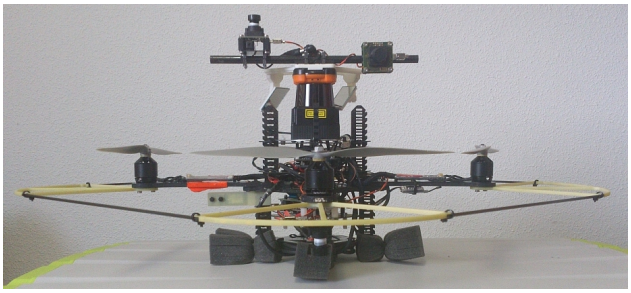

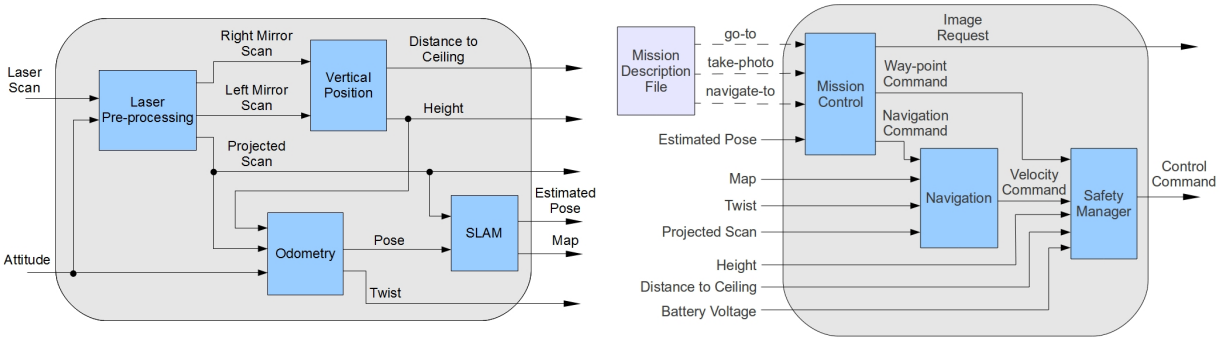

(b) (c)

(d)

```
1  <mission>
2  <goto x="0.0" y="0.0" z="1.0" spx="0.2" spy="0.2" spz="0.2" yaw="0.79" accpos="0.1" accori="0.0" timeout="30" stay_time="5.0" />
3  <takephoto camera="1" path="picture1.jpg" stay_time="5.0"/>
4  <goto x="2.0" y="0.0" z="1.0" spx="0.2" spy="0.2" spz="0.2" yaw="0.79" accpos="0.1" accori="0.0" timeout="30" stay_time="5.0" />
5  <takephoto camera="1" path="picture2.jpg" stay_time="5.0" />
6  <goto x="0.0" y="0.0" z="1.0" spx="0.2" spy="0.2" spz="0.2" yaw="0.79" accpos="0.1" accori="0.0" timeout="30" stay_time="5.0" />
7  <goto x="0.0" y="0.0" z="0.0" spx="0.2" spy="0.2" spz="0.2" yaw="0.79" accpos="0.3" accori="0.0" timeout="30" />
8  </mission>
```

Figure 3: The aerial vehicle: (a) platform overview, (b) self-localization and mapping modules, (c) mission execution modules, (d) example of a mission specification file.

also reported by other authors (Achtelik et al., 2009) to permit autonomous flying. Furthermore, information exchange between the laptops is performed by wire and the wireless datalink is left only for communication with the MAV. That is to say, only one laptop talks directly with the MAV, which reduces multiple point-to-point communications for the same data, but they are republished by this laptop to provide the full cluster with all the information. This configuration permits adding new computers to the cluster as needed, ensuring there is no extra wireless communication with the vehicle. For more details about the MAV control software, refer to (Bonnin-Pascual et al., 2012).

3.3 Lightweight Inspection Robot for Stage 2

3.3.1 General overview and design of the robot

The lightweight climbing robot is depicted in Fig. 4. It is actuated by two 12 V DC motors that drive the two front wheels, on which a total of 112 neodymium magnets are attached. The adhesion force on an iron surface is 12.16 N per magnet. The polarities of the magnets are oriented alternately to increase the adhesion force. Each wheel consists of two rows of magnets with a foam material applied in between, to increase the traction during climbing. The magnets are integrated into flexible rubber holdings which provide adaptability to the surface, and allow the system to traverse between surfaces. Furthermore, a tail is attached to the system using a flexible tail joint. During wall climbing, the tail bends around the z-axis, allowing motion in circles with a small radius. At the tail tip, a rocker has been incorporated with two additional magnetic rings. This provides an additional degree of freedom that allows the tail wheels to adapt

to uneven parts and climb on corrugated metal parts. Finally, since the system weight is well below 1 kg, no safety precautions need to be taken, except for a small catching net to be used by a second person to catch the robot in case it drops from, e.g., a bulkhead, in contrast to many existing magnetic climbing robots which need to be secured by a crane or a safety rope. As a result, the system can be quickly deployed to obtain visual close-up data from areas that are hard to reach. To provide visual data, a camera is attached to the front of the robot, including an LED light

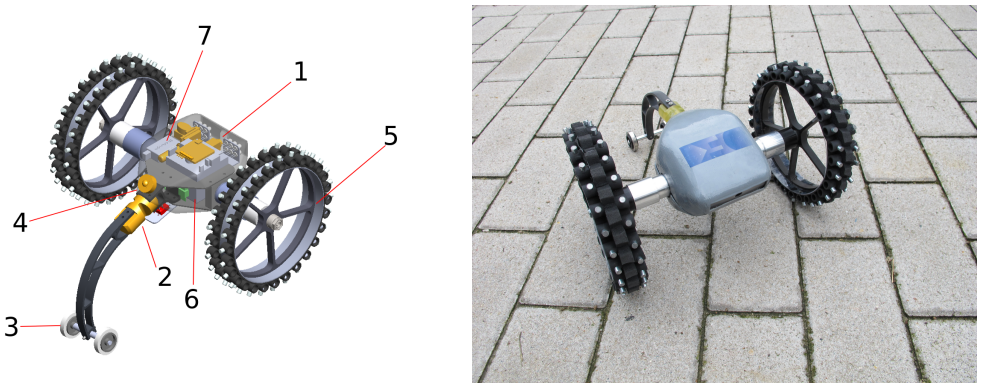

Figure 4: The lightweight crawler: (a) isometric view, with 1) video camera and LED light source, 2) elastic tail joint, 3) magnetic rear wheel rocker, 4) high-power LED for position tracking, 5) magnetic front wheel, 6) 12V LiPo battery pack, and 7) 2.4GHz M-PCM receiver; (b) vehicle realization.

source to enhance the image quality. The robot also stores high resolution images and video streams directly on a local SD-card for post-processing. The lightweight crawler is also capable of marking defects directly on the bulkhead of a ship, using a micro-pump to apply acrylic varnish on the surface. See (Eich and Vögele, 2011) for more details on the design of the lightweight crawler.

3.3.2 Control architecture

This section describes the control software of the lightweight inspection system, a graphical overview of which is shown in Fig. 5. As can be observed, the diagram also includes the SCMS, although the corresponding details will not be given until Section 5, since it is a system which is orthogonal to the robot team. We include the SCMS in this discussion to illustrate how, in particular, the lightweight crawler interacts with it. Any other platform interacts in approximately the same way, thanks to the modularity principles that have been adopted for the design of the full inspection system[1]. With regard to the lightweight inspection system in particular, the operator controls the robot using a 2.4 GHz M-PCM RC unit which provides the speed signal to the motors, and gets direct feedback from the robot via a first-person-view (FPV) interface. The remote control also provides a PCM interface to the control computer, allowing different control modalities, e.g., direct control by an operator, where the robot receiver sends the commands to the DC drivers; or indirect control by a navigation algorithm. The pump spray unit is actuated using a micro-actuator, which is also directly triggered via the RC. The FPV interface is implemented through an analog wireless 5.8 GHz link. During field trials, two different options were evaluated (see Fig. 6): hand-held devices and video goggles, the latter providing the operator with an immersive view in the scenery through the camera of the robot. Because maneuvering the robot only from the FPV can cause nausea, especially if the robot is at a significant height, it has been observed that it is desirable that a direct line of sight exist between the operator and the robot.

3.3.3 Associated vision-based localization unit

Due to the size and weight of the lightweight crawler, which were directly imposed by the requirements, the system cannot carry additional sensors that could be used to derive its position. However, in Stage 2, metric localization is mandatory in order to localize the acquired data. The 3D localization system and the control architecture are shown in Fig. 7. In this diagram, U corresponds to the camera's horizontal image resolution and V to its vertical one. The

[1]The same would apply to the optical tracking unit and the heavyweight crawler.

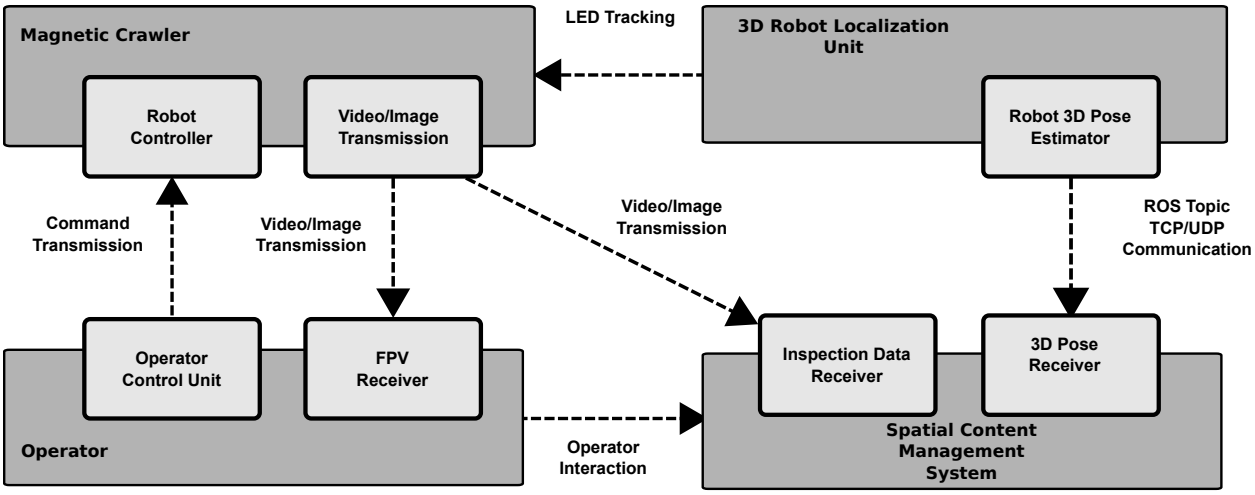

Figure 5: Overview of the control software of the lightweight inspection system. Besides the operator as man-in-the-loop, the system architecture comprises the mobile robot and the 3D localization unit. The drawing also gives the relation between the lightweight crawler and the SCMS.

Figure 6: User interfaces for the FPV of the lightweight inspection system: (left) small and portable handheld 5-cm screen device; (center) custom developed screen box comprising a 5.8 GHz video receiver and an 18-cm TFT screen; (right) full immersive video goggles used by the surveyor during field trials.

camera is in the fixed reference frame of the laser range finder, and both are actuated, in accordance with the estimated pitch and yaw angles (θ, φ) of the target, by the two servo motors of the pan-tilt unit (PTU). The image provided by the camera is pre-processed using a Laplacian of Gaussian filter (LoG) (Haralick and Shapiro, 1992). The resulting image $g(u, v)$ has steep intensity gradients and is well suited to detect the bright light source of the LED in the images. The output of the detector is the position (u, v) of the center of gravity (CoG) of the image. Common problems when tracking a light source are that the position might jump to other bright sources during the tracking process, or the target itself can get temporarily occluded.

Due to its well-known robustness to multi-modal distributions and occlusions (Isard and Blake, 1998), we have adopted a Monte Carlo particle filter which is used in combination with sequential importance re-sampling (SIR). The method we use for the blob estimation in the image plane is a variant of the sample-based Monte Carlo localization (MCL) method, which is well-known for robot pose tracking within a 2D map (Thrun et al., 2000). In general, the following recursive equation is solved using the particle filter in order to estimate the position of a system (μ is a normalization factor):

$$Bel(x_t) = \mu \frac{1}{\sigma\sqrt{2\pi}} e^{-\frac{1}{2}\left(\frac{\|o_t - x_t\|}{\sigma}\right)^2} \int p(x_t | x_{t-1}, \mathcal{T}(x_{t-1}, x_{t-2}), g(x_{t-1}, \sigma)) Bel(x_{t-1}) \mathrm{d}x_{t-1} \quad (1)$$

In contrast to the application of the particle filter in robot localization, no direct action update a is available to the

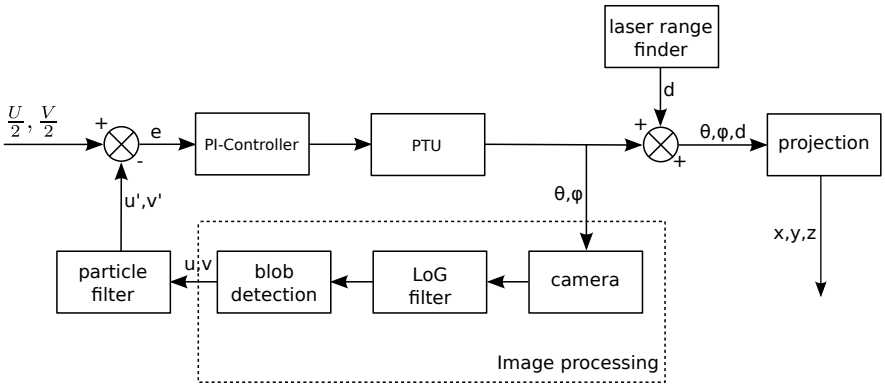

Figure 7: 3D localization unit: (left) integrated system; (right) control architecture.

system, therefore we estimated the last action by the translation between the two positions. To account for the change of speed and direction between two pose estimation steps, we add Gaussian noise into the motion model. The last motion at time x_{t-1} is thus based on the translation between the two prior estimated positions, $\mathcal{T}(x_{t-1}, x_{t-2})$. The Gaussian noise is incorporated as the function $g(x_{t-1}, \sigma)$. In our case, we take the distance between the estimated position and the new blob measurement given by the blob detection algorithm.

In the sequential importance re-sampling step, each sample is redrawn from the sample set according to its weight $\omega^i = \mu \frac{1}{\sigma\sqrt{2\pi}} \exp(-\|o_t - x_t^i\|^2/(2\sigma^2))$, which arranges that good samples are reproduced while samples with a low likelihood are removed from the set[2]. The output of the system is, thus, the 3D position of the robot in polar coordinates, which is projected onto the reference frame of the tracker using $x = d\sin\theta\cos\varphi$, $y = d\sin\theta\sin\varphi$ and $z = d\cos\theta$. This estimate is regularly provided to the operator and to the SCMS.

3.4 Heavyweight Inspection Robot for Stage 3

3.4.1 General overview and design of the robot

As mentioned before, unlike the lightweight climber, this crawler requires a larger payload capacity in order to carry an electrical robotic arm and an ultrasound probe for non-destructive thickness measurement, apart from other sensors and devices. As a consequence, the mechanical design of this heavier vehicle has been essentially determined by the choice of the climbing system. In order to minimize the risk of detaching and crashing while using a passive adherence system, magnetic tracks were preferred to wheels in virtue of their ability to maximize the contact area with the metal surface. The result was the Magnetic Autonomous Robotic Crawler (MARC) shown in Fig. 8.

As can be seen, a cart, actuated by a DC brushless servomotor and rigidly connected to a couple of wheels, has been mounted at the rear of the vehicle. The wheeled cart, positioned in *home*, *up*, and *down* configurations, as shown in Fig. 8, helps the vehicle to cross slope discontinuities and to not overturn when working on vertical slopes. As far as the magnetic tracks are concerned, custom-made platelet-shaped magnets have been designed, built, and directly fixed to the holes of the track chain brackets. Each magnet, which measures 40 × 22 mm, exerts a maximum magnetic force of about 100 N. Since, under nominal operating conditions, 8–10 magnets per track are in contact with the metallic surface, the corresponding attractive force is of 800–1000 N per track (1600–2000 N in total). Each track is actuated by a 140 W brushless motor coupled to a gearhead with reduction ratio 85:1 for a resulting maximum speed of 0.12 m/s. Motors and gear-boxes are mounted at the bottom part of the vehicle, together with Li-Ion battery packs placed along the longitudinal axis and at the rear part of the platform.

[2] μ ensures the weights ω^i sum up to 1

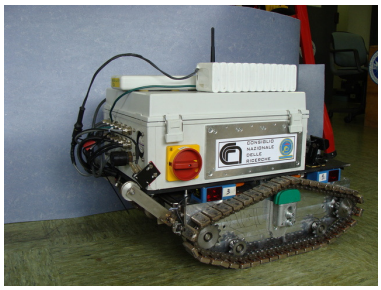

(a) Wheels in *home* position: used for operations over non-vertical slopes

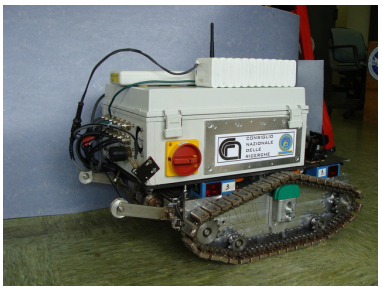

(b) Wheels in *up* position: used for handling slope discontinuities between 45 and 90 degrees.

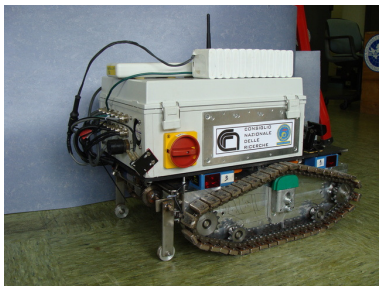

(c) Wheels in *down* position: used when working on vertical slopes.

Figure 8: MARC rear wheel configurations.

3.4.2 Control architecture

The MARC sensor system consists of: a high performance, miniature attitude heading reference system (AHRS) with GPS, combining MEMS sensor technology and a highly sensitive embedded GPS receiver, providing orientation, inertial, and, when possible, GPS measurements; and four laser range sensors, able to measure the distance to, e.g., lateral bulkheads, and allowing the computation of the platform's position and orientation inside an operating lane. The vehicle-embedded real time computing platform is based on commercial-off-the-shelf (COTS) hardware and free software: in particular, a single-board computer hardware architecture, possessing PC-compatible CPUs, has been adopted to support a Linux-operated system configured for real time performance as discussed in (Bruzzone et al., 2009).

The MARC control system is able to follow a linear surface on the basis of lateral range measurements. The measurements provided by the pair of laser range sensors mounted perpendicularly to the vehicle side allow estimating the distance d and orientation φ of the vehicle with respect to a linear vertical shell frame. The proposed control law for following a linear surface, using a simple Lyapunov-based design, is

$$\begin{cases} u = u^* \\ \dot{\varphi} = -k_d u^* (d - d^*) - k_\varphi \sin \varphi \end{cases} \tag{2}$$

where u^* is the linear reference speed of the vehicle, $\dot{\varphi}$ is its yaw rate, d^* is the reference range from the tracked linear surface, d is the current distance to the surface, and k_d and k_φ are positive constants. This allows MARC to follow a linear surface at a reference range, remaining parallel to the tracked surface. See (Bibuli et al., 2012) for more details about MARC.

3.4.3 Associated robotic arm for NDT measurement

Given the complexity of ship structures and their common environmental conditions, e.g., highly corroded, rusted or even bent structural members, ultrasonic thickness measurement (UTM) becomes a tedious task even for skilled UT operators, involving a number of phases: surface preparation, which can become the longest task since it is not uncommon to have significant scale and rust on the metallic surface; application of couplant, usually a high viscosity liquid, such as glycerin, whose purpose is to increase the transmission coefficient of the medium traversed by the ultrasonic pulse that goes from the probe to the uneven surface of the specimen; and UT probe application and measurement, which can require additional surface preparation if the UTM is not steady or if unreliable readings are obtained. Due to these conditions, and in order to require only a minimum of skills from the user, the robotic arm carried by MARC exhibits a certain degree of adaptability and intelligence in order to allow the measurement of a wide range of significant ship structural components, such as frame stiffeners, brackets, and face plates, as required by the classes. Five degrees of freedom (4 angular and 1 linear), a holding torque of 1 kg/m (@18.5V) and an angular resolution of 0.3° are the key resulting specifications of the arm at the mechanical level. Regarding the arm controller, it features a USB interface with MARC and an ARM Cortex M3 (@72 MHz) processor, running a 400 Hz control

loop which in particular implements spline-based trajectory following. Finally, about the end-effector, it comprises a grinder for surface preparation (using current monitoring for torque control), a peristaltic pump to inject the couplant that improves the transmission of the ultrasonic pulse, and the corresponding ultrasound sensor. Referring particularly to the task of thickness measurement, the robot is equipped with an FPGA-based board responsible for the high voltage pulse generation ($<$ 390 V), the return signal amplification (0–100 dB), and the digitization at a maximum sampling rate of 100 MHz and 10-bit resolution. For a more detailed description, refer to (Koveos et al., 2012). UTM relies on measuring the time for an ultrasonic pulse to propagate along the material under test and extract its thickness on the basis of the speed of sound c. It is typical from NDT to use A-Scan waveforms, i.e. ultrasonic amplitude *versus* time of arrival, for visual inspection. However, since the raw waveform is usually noisy and may contain signals from multiple reflections, time is measured from a filtered signal, y_n, representing the energy of the ultrasound. This is obtained by low-pass filtering a rectified input signal x_n.

Since the waveform is buffered, a zero-phase formulation is used to preserve phase information (in the following, P and Q are, respectively, the feedforward and the feedback filter orders, b_i and a_i are the corresponding filter coefficients and N is the number of samples):

$$\begin{array}{ll} \text{1) Forward filtering:} & y_n^* = \frac{1}{a_0}\left(\sum_{i=0}^{P} b_i \left|x_{n-i}\right| - \sum_{j=1}^{Q} a_j y_{n-j}^1\right),\ n = 0\,..\,N \\ \text{2) Reverse-time filtering:} & y_n = \frac{1}{a_0}\left(\sum_{i=0}^{P} b_i y_{N-n-i}^* - \sum_{j=1}^{Q} a_j y_{n-j}\right),\ n = 0\,..\,N \\ \text{3) Time reversing:} & y_n = y_{N-n},\ n = 0\,..\,N \end{array} \tag{3}$$

Regarding thickness calculation, it can be implemented through a peak detection algorithm: leveraging the fact that ultrasonic echoes are monotonically decreasing due to absorption and reflection losses, time of flight can be estimated as the time between those peaks. Despite this method being simple, it relies on single points of the waveform and is subject to variations of the user selected parameters, e.g. filter bandwidth, amplification, etc. A second algorithm, based on the auto-correlation of the unfiltered input signal, is preferred instead. Although more computationally intensive, it provides robust estimations due to the use of the entire waveform, minimizing any dependency on the user-provided parameters, and augmenting the level of autonomy. The thickness is then estimated as follows:

$$\text{thickness} = \frac{c}{2}\,dt\left(\arg\max_j \sum_n x_n x_{n-j}\right),\ j \in n_{min}\,..\,n_{max}\,, \tag{4}$$

with dt the sampling period, and n_{min} , n_{max} defined by the minimum and maximum measurable thicknesses, which, in this work, come from a wide range 3–30 mm, satisfying the survey's requirements, typically 5–25 mm.

4 A vision-based solution for defect detection

This section proposes a vision-based integrated solution for detecting two kind of defects of metallic surfaces that are generally considered relevant to determining the condition of a vessel, namely, coating breakdown/corrosion and cracks. (Bonnin-Pascual, 2010) performs a thorough review of the different techniques which have been used so far for defect detection in general. Some of those proposals are specifically related to vessel inspection, although they mostly refer to the inspection of the external part of the hull by means of (mainly tethered) unmanned underwater vehicles. Their main goal is to assist with the detection of the loss of the external coating, aquatic life adhering to the hull (to prevent future corrosion), artificial objects attached to the hull (to avoid sabotage), weld inspection, etc.

The approach described in this section aims at detecting the aforementioned defects from the digital images captured by the MINOAS robotic platforms. It must be regarded as an assistance tool in the hands of the surveyor, which essentially means there will always be a human making the last decision about the state of the corresponding structural component. In more detail, the defect detector is an integrated solution that considers both kinds of defect through an algorithm comprising two stages. The first stage, corrosion detection, is in charge of labeling all areas of the input image suspected of being affected by corrosion. The second stage, crack detection, makes use of the pixels classified as *corroded* as clues for detecting cracks. The rationale behind this approach comes from the observation that, typically, in metallic surfaces, cracks are surrounded by corroded areas, so that guiding the crack detector in accordance with

the output of the corrosion detector becomes a highly effective strategy for enhancing its performance. The two stages are outlined in the following sections. For more details, see (Bonnin-Pascual, 2010).

4.1 Corrosion detection

The corrosion detector is based on a supervised classification scheme that comprises two steps that can be considered as two weak classifiers. The idea is to chain different fast classifiers with poor performance in order to obtain a global classifier attaining a higher global performance. The first classifier is based on the premise that a corroded area exhibits a rough texture. Roughness is measured as the energy of the symmetric gray-level co-occurrence matrix (GLCM), calculated for downsampled intensity values between 0 and 31, for a given direction α and distance d. The *texture energy* E is defined as $E = \sum_{i=0}^{31} \sum_{j=0}^{31} p(i,j)^2$, where $p(i,j)$ is the probability of the occurrence of gray levels i and j at distance d and orientations α or $\alpha + \pi$. Patches with an energy lower than a given threshold τ_E, i.e., those which exhibit a rough texture, are finally candidates to be more deeply inspected.

The second classifier operates over the pixels of the patches that have survived the roughness step. This classifier makes use of the colour information that can be observed from the corroded areas, unlike the first classifier. It works over the hue-saturation-value (HSV) space after the realization that HSV-values that can be found in corroded areas are confined to a bounded subspace of the HS plane. Although the V component has been observed to be neither significant nor necessary to describe the color of the corrosion, it is used to prevent the well-known instabilities in the computation of hue and saturation when the color is close to white or black. This second step requires a prior training step to learn the color of the corroded areas, which consists in building a bidimensional histogram of HS values for image pixels labelled as 'corroded'. The resulting histogram is subsequently filtered by zeroing entries whose value is below 10% of the highest peak, and, next , applying a bilateral filter, considering the bins' heights as the intensity values of a digital image. This approach filters the histogram using a kernel consisting of two Gaussians, one for the spatial domain and another for the range domain. The colour classifier proceeds as follows for every 3-tuple (h, s, v): given thresholds mV, MV and mS, pixels close to black, $v < mV$, or white, $v > MV \wedge s < mS$, are labelled as non-corroded, while the remaining pixels are classified as corroded if the HS histogram contains a non-zero value at the (h, s) entry.

4.2 Crack detection

The crack detector proceeds in accordance with a percolation model, similarly to the approach described in (Yamaguchi and Hashimoto, 2010), although their detector was constructed for searching cracks in concrete; this fact makes the authors assume a geometrical structure that does not match exactly the shape of the cracks that are formed in steel. The percolation model used is developed from a region-growing procedure which starts from a seed pixel and propagates in accordance to a set of rules. In our case, the rules are defined to identify dark, narrow and elongated sets of connected pixels, which are then labelled as cracks. Once a seed pixel has been defined, the percolation process starts as a two-step procedure: during the first step, the percolation is applied inside a window of $N \times N$ pixels until the window boundary is reached; in the second step, if the elongation of the grown region is above ϵ_N, a second percolation is performed until either the boundary of a window of $M \times M$ pixels ($M > N$) is reached or the propagation cannot progress because the gray levels of all the pixels next to the current boundary are above a threshold T. Finally, all the pixels within the region grown are classified as crack pixels if the region elongation is larger than ϵ_M.

Within the $N \times N$- or the $M \times M$-pixel window, the percolation proceeds in accordance to the next propagation rules: (1) all 8 neighbours of the percolated area are defined as candidates, and (2) each candidate p is visited and included in the percolated area only if its gray level value $I(p)$ is lower than a threshold T, which has been initialized to the seed pixel gray level. At the end of the percolation process, the mean gray level of the set of pixels is checked to determine if the region is dark enough to be considered a crack; otherwise, the region is discarded, and another percolation starts at a different seed pixel. Seed pixels are defined over a regular grid with a step of Δ pixels, and are required to coincide with an edge whose gray level is below γ_s. To ensure that the relevant edges are always considered, a dilation step follows the edge detection, where the dilation thickness is in accordance with Δ. Furthermore, since the crack detector operates under the guidance of the corrosion detector, as mentioned above, seed pixels are required to

lie within corroded areas. The different conditions for being a seed pixel, taken together, speed up the crack detection process and reduce the false positive rate thanks to the corrosion-based guidance.

5 Spatial Content Management System for Robot-acquired Inspection Data

Classification societies use software packages such as the Germanischer LLoyd HullManager [3], which provides the means to assess the ship's condition and store the relevant data for later use. Mobile tools for damage assessment also exist from Sertica[4]. With this tool, the surveyor can incorporate inspection data using a portable device. Publications regarding inspection data management tools can be found in (Fletcher and Kattan, 2009). All these tools, however, require an operator who manually inputs the inspection data.

The SCMS that is introduced in this section integrates the surveyors and the inspection robots in a sort of man-in-the-loop strategy. The inspection data acquired by the robots, are collected with the SCMS and can be evaluated during or after the inspection. Currently, no system of this kind is available. The SCMS is a central element of the inspection system which is proposed in this work. In more detail, it permits collecting, sharing and displaying in a centralized manner all the information gathered using a 3D representation of the vessel under inspection. All robot systems introduced in this paper can provide images, videos or thickness measurements during the inspection to the SCMS using common interfaces. As mentioned in (Caccia et al., 2010a), a surveyor does not use a metric representation for localizing inspection data, but rather uses the spatial topology of the ship, i.e., "cargo hold 1, port side, bulkhead, left side": inspection data are topologically assigned to the named parts of the ship within the SCMS. The ship as a whole is thus internally represented as a tree structure, each node corresponding to a certain part of the ship. The 3D interface of the SCMS is shown in Figure 5. The data is internally assigned to the topological parts of the vessel (cf.

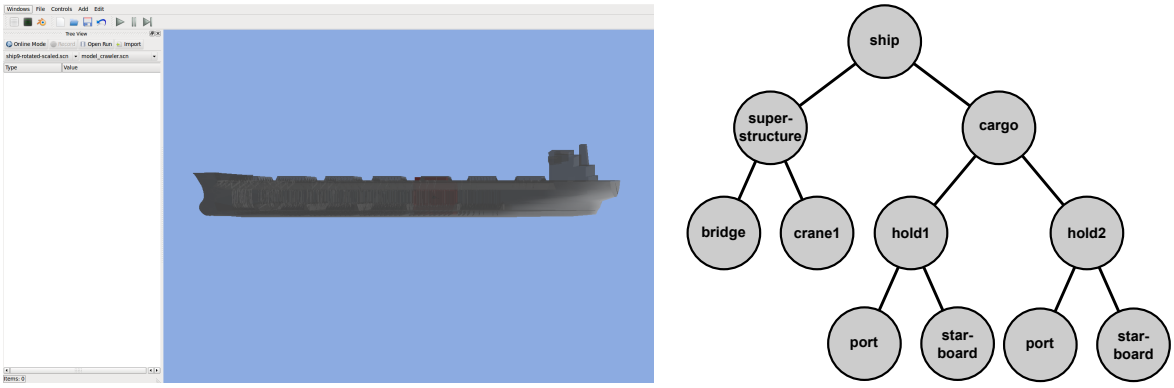

Figure 9: The Spatial Content Management System: (left) The 3D user interface. (right) The data is internally assigned to topological parts of the vessel. Within the nodes, the localization of the data is performed metrically.

Figure 5). The inspection data are anchored to the nodes of the tree structure. This representation as a graph, apart from being logical to the users, allows a quick access to the data, since all the inspection data for a certain topological unit, e.g., a certain cargo hold, are located under a certain branch of the tree structure. Nevertheless, the location of the inspection data is also represented in a metrical way within the data node leafs, each leaf node having its own local, metric reference frame aligned to the 3D representation of the ship. The origin of the reference frame corresponds to a fixed position, e.g., where the localization unit was placed during the inspection, with the only constraint being that, across surveys, approximately the same position must be used. Within the SCMS, the surveyor navigates through a 3D model of the ship to get access to the different areas, while the inspection data items are projected metrically into the 3D model as data blobs which can also be selected by the surveyor. Furthermore, all the data associated to a certain node, irrespective of their modality and recording date, are available once the item is selected. Finally, 3D sub-models

[3] http://www.gl-maritime-software.com/gl-hullmanager.php
[4] http://www.sertica.dk/

can be associated to each tree node in order to obtain a higher level of detail of the corresponding structural element when selected.

6 Systems performance evaluation

The marine inspection system described in this work was tested both in the laboratory and in field trials. This section reports the results collected for every platform during the different experiments that were performed. The first trial was performed on a bulk carrier ship which was under repair in a shipyard in Varna, Bulgaria. Several ship surveyors attended the trials and provided comments on the usability of the various platforms and on possible improvements. The second trial was also performed on a container cargo ship in the same shipyard which served also as a final validation point for all systems. The two test cargo holds are shown in Fig. 10.

Figure 10: Vessel holds involved in the first and the second field trials: (left) cargo hold of the bulk carrier after it was cleaned, and (right) cargo hold of the container ship.

6.1 Performance of the aerial platform

This section reports on the results of a number of laboratory and field experiments to demonstrate the navigation capabilities of the MAV. These experiments were planned to cover the kind of capabilities required to perform Stage 1 of a MINOAS inspection mission. To begin with, Fig. 11 shows results for the MAV operating in semi-autonomous mode, with the operator trying to reach, with the assistance of the platform, a set of waypoints within a laboratory of the University of the Balearic Islands (see Fig. 11(a) and (c)) and during the first field trial onboard the bulk carrier ship (see Fig. 11(b) and (d)). As can be noticed, the platform effectively provides the operator with height control and hovering functionalities. The first experiment in autonomous mode that is reported, whose results are provided in Fig. 12(a–d), shows the ability of the platform to reaching, without the intervention of an operator, a number of waypoints at different heights (within a building of the University of the Balearic Islands). More precisely, the mission describes a wall sweeping task, as would be done onboard a ship, although at the scale of a laboratory. The mission consists in attaining, with an accuracy of 0.1 m, a total of ten waypoints along a zig-zag path, as indicated in Fig. 12(b). A different kind of experiment (also performed within a building of the University of the Balearic Islands) is shown in Fig. 12(e–h). In this case, apart from reaching a set of waypoints autonomously, the goal is to perform two short sweeping tasks in adjacent rooms, so that a safe path through the door communicating booth rooms has to be planned and followed during the flight. That is to say, in this experiment, the MAV faces all the difficulties of a real scenario. As well as in the previous experiment, the different waypoints are correctly attained—within the accuracy requirements determined by the mission specification file (0.1 m)—while the local and global path planners produce safe paths towards the targets.

A third set of experiments in autonomous mode taking place onboard the container ship, during the second field trial, is here reported (see Fig. 13(a)). This time the mission description file specified a sweeping task, consisting in reaching

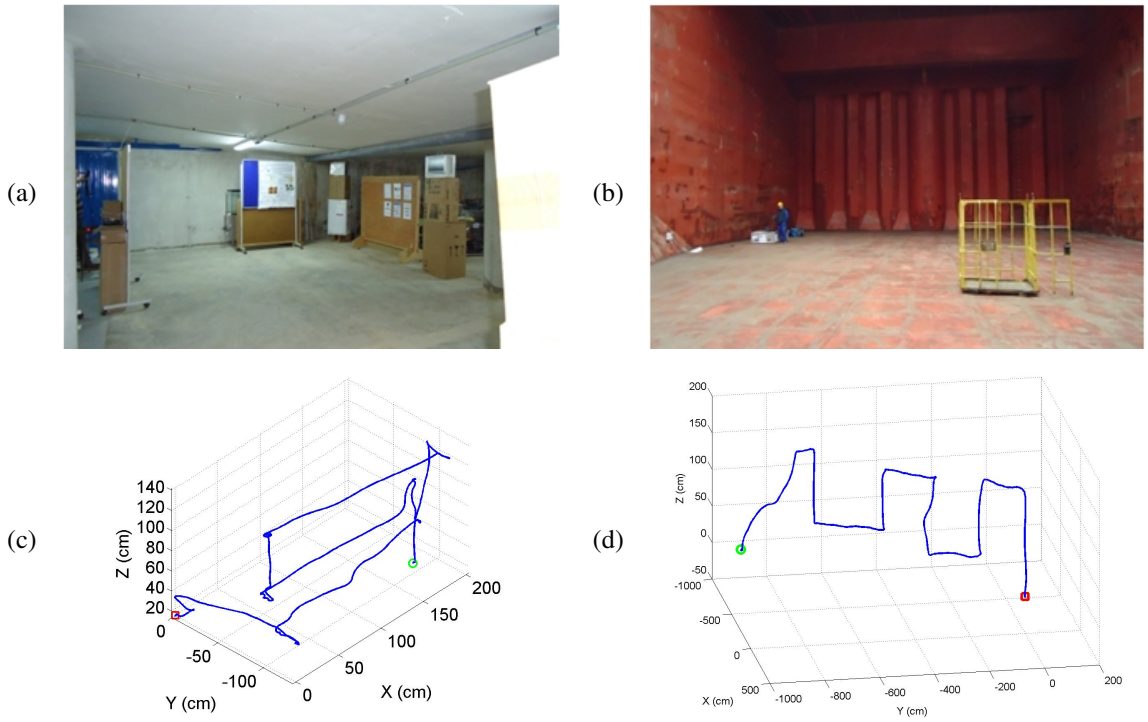

Figure 11: The MAV operating in semi-autonomous mode: (a,b) snapshots of the environments; (c) path followed by the MAV during the laboratory experiment; (d) path followed by the MAV during the field trial. (The red square indicates the take-off position and the green circle, the landing position.)

a collection of sixteen waypoints along a zig-zag like path (see Fig. 13(b)), and the experiment was performed several times to compare the results of the consecutive executions. The results, which can be found in Fig. 13(c–d), show that (1) the paths estimated by the vehicle are consistent with the environment, as well as the map built by the laser-based SLAM component, and (2) the behaviour of the MAV is repeatable (up to the accuracy requested in the mission specification file, 0.1 m), both of which suggest the validity of the navigation approach. Pictures taken by the onboard cameras at some of the waypoints can be found in Fig. 13(e).

6.2 Performance of the Lightweight Inspection System

6.2.1 Lightweight crawler

As for the climbing capability of the robot, several tests were performed over mainly vertical bulkheads, and also along 70° slopes. Fig. 14(a) shows the climbing robot on a slope and Fig. 14(b) on a transverse bulkhead. In this regard, Table 2 shows the maximum tear-off force against the maximum vertical drag force exerted by the robot while climbing vertically on a bulkhead along a straight line. The reference measurement for the robot was taken while climbing a clean, bare steel frame without any coating. The system was able to create a lift of 19.8 N while climbing vertically. The wheels of the robot blocked because the motors were not able to create more torque. Therefore, this number corresponds to the maximum lift the robot could produce under optimal conditions. The maximum tear-off force was measured as 45.1 N. In all the experiments, except the reference measurement, the wheels started to slip and the magnets could not produce enough adhesive force for the robot to move upward. A live image of the crawler was received by the small hand-held device depicted in Fig. 6(left). In contrast to the laboratory experiments, the 2.4 GHz analog video signal suffered from several problems, being significantly distorted at a distance of more than three meters. Because of the video transmission issue, only the videos and images stored directly on the robot could be used by the surveyor. Of particular relevance in this regard is the fact that the robot was able to take high-quality snapshots

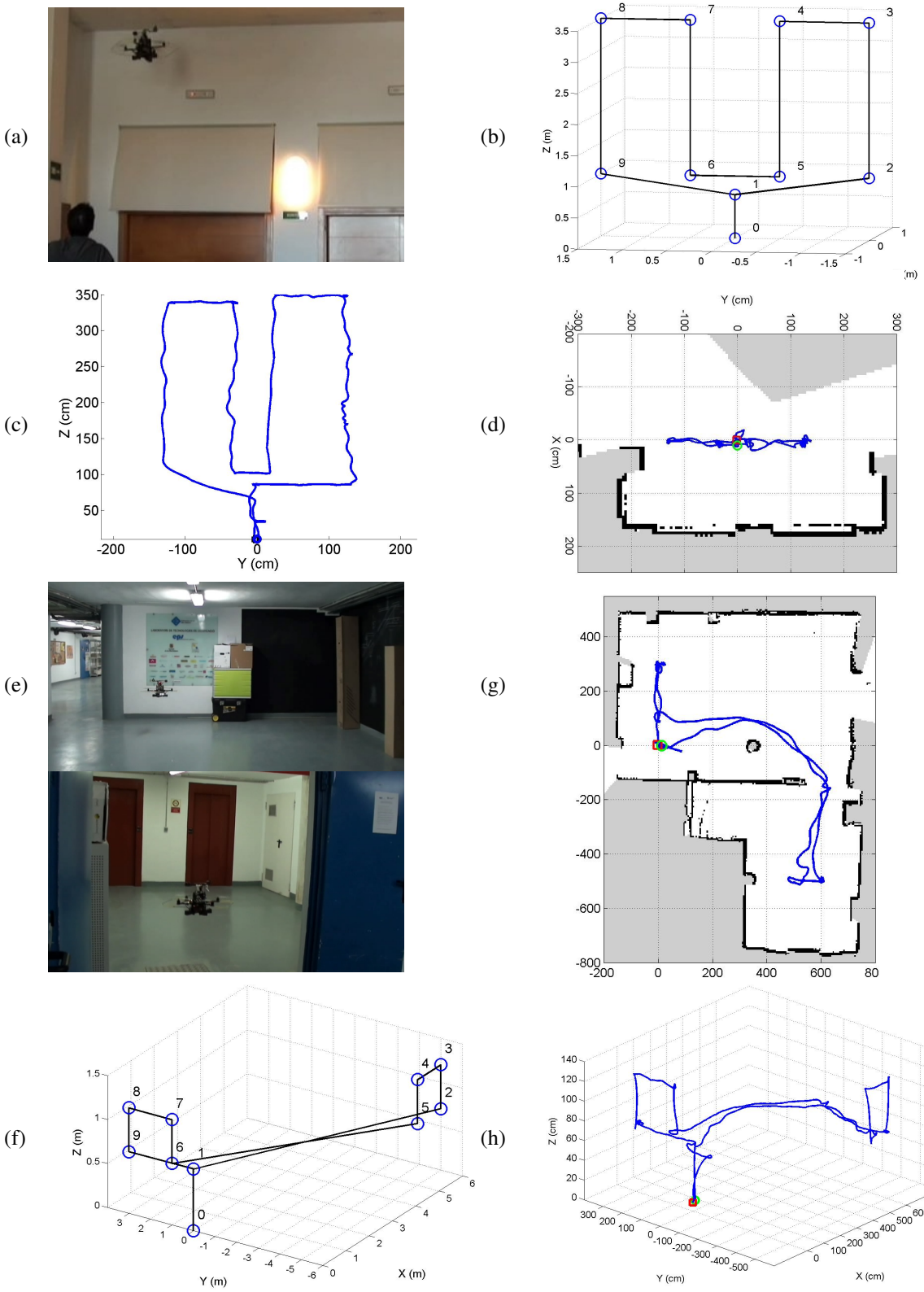

Figure 12: MAV results in autonomous mode under laboratory conditions: [1st experiment] (a) snapshot of the environment, (b) sequence of waypoints to be reached: 0–9/1/0, (c) path followed by the MAV, and (d) 2D path followed by the MAV superimposed over part of the map; [2nd experiment] (e) snapshots of the two rooms where the experiment takes place—the MAV departs from *above*, goes *below*, and finally returns *above*—, (f) sequence of waypoints to be reached: 0–9/1/0, and (g–h) map and 2D/3D path followed by the MAV.

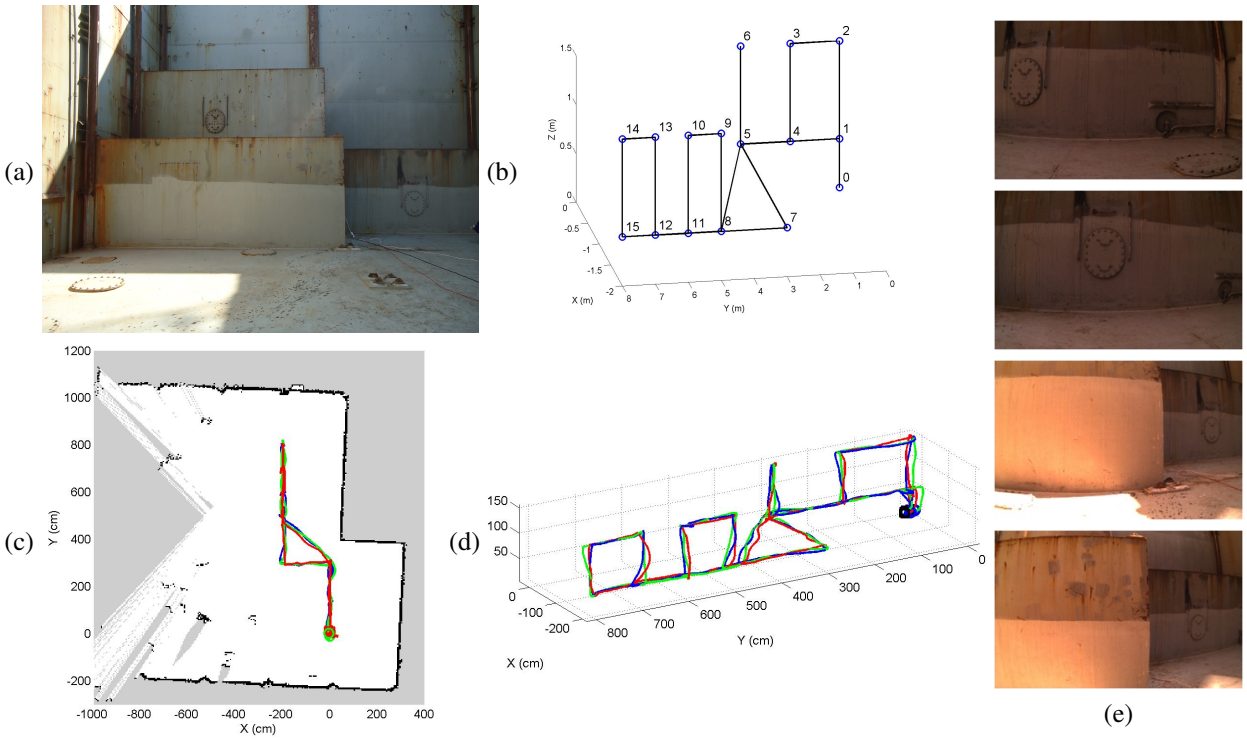

Figure 13: MAV results in autonomous mode from the second field trial: (a) hold area where the experiment takes place, (b) sequence of waypoints to be reached by the MAV: 0–6/5/7–15/8/5/1/0, (c-d) map and 2D/3D paths followed by the MAV, and (e) pictures taken at waypoints 1, 4, 8 and 9 [from top to bottom].

Table 2: Performance of the climbing robot on different vertical surfaces

Surface	Condition	Max. Vertical Drag Force (N)	Max. Tear-off Force (N)	Robot Behavior
5 mm bare steel plate	clean	45.1	19.8	block
1 mm sheet metal	clean	25.5	12.4	slip
coated steel	clean	30.3	15.7	slip
coated steel	corrosion	28.6	12.2	slip
bare steel	corrosion	25.5	17.1	slip

of some damage at some welding seams which were of interest to the surveyors because the damage was not visible to the surveyor without using the robot (cf. Fig. 14(c–e)). The quality of the images was sufficient to estimate the level of corrosion. The experimental setup during the trial within a container hold, which involved a surveyor, an operator, the 3D tracking unit, and the lightweight crawler, is shown in Fig. 15(a). The robot was constantly sending images to the SCMS, which was running on a laptop. Some snapshots of the transmitted images are shown in Fig. 15(c) and 15(d). To check the performance of the crawler, an operator within the line of sight controlled the robot, while the surveyor would indicate where to move. The robot was able to climb on the vertical walls of the cargo hold. Besides, it was useful for inspecting the spaces behind the guidance rails for the containers (see Fig. 15(b)) that were not visible to the surveyor without using the robot. However, rust and dirt would stick to the magnets, causing problems for the crawler (see Fig. 15(e)).

Summarizing the trials, we can say that on the one hand, the main strength of the lighweight crawler is its ease of use, which was proved by the surveyors themselves' being able to control the robot without prior training. Even without the tracking system and the SCMS, the robot alone proved able to serve as an extension of the surveyor's eyes, supplying him with a quick look at parts of the ship which otherwise are accessible only using staging or cherry-picking methods. On the other hand, the second trial also showed clearly the limits of using a magnetic climbing

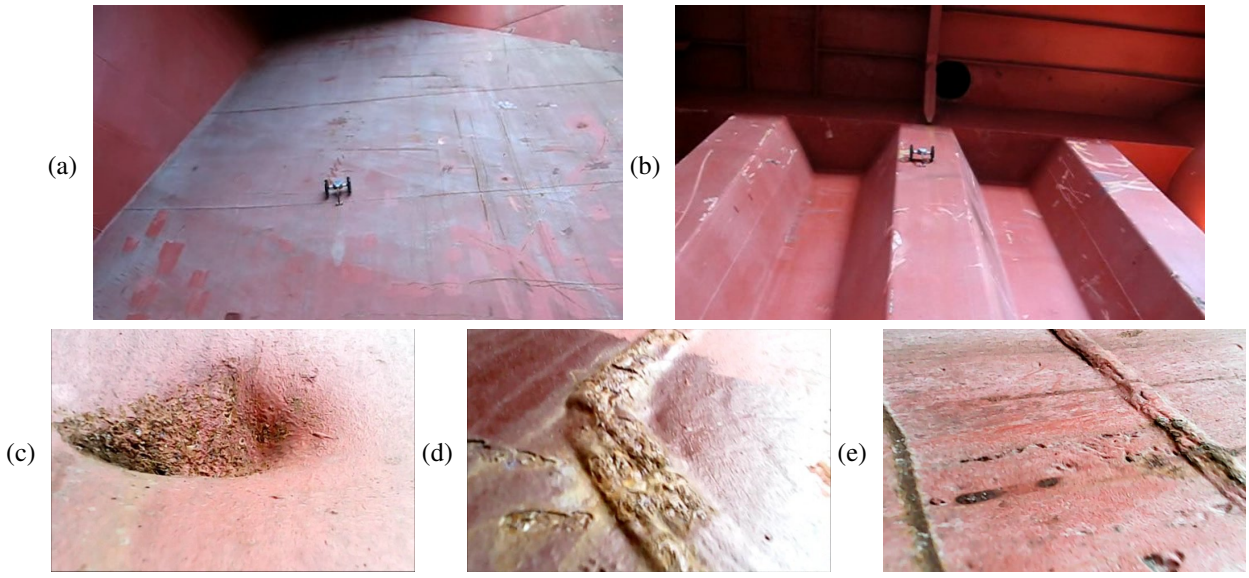

Figure 14: First trial for the lightweight crawler: the climbing performance was tested on a 70° slope (a), as well as on a vertical transverse bulkhead (b); (c-e) sample images taken by the robot.

system in a real environment: rust and dirt did not allow the crawler to climb freely on the bulkhead, although it was possible for the operator to navigate the robot around such critical patches. Since rusty patches provide less adhesion force for magnets, a system with stronger magnets would solve the problem, such as the heavy weight crawler MARC described in this paper. The heavy weight crawler had no problems in heavily corroded bulkheads, but on the other hand, needed more safety precautions and more setup time.

6.2.2 Localization experiments

In this section, we report the performance of the 3D tracking unit while tracking the lightweight crawler. To this end, the absolute error was measured and compared with a reference value of 0.3 m. This value comes from the structure of cargo holds in different sorts of vessels (e.g., bulk carriers and containerships), and corresponds to the average distance between the sections in which bulkheads and walls are typically divided. In this way, the surveyor can know the section from which the inspection data were taken. During the experiments, the crawler would move along a vertical bulkhead of the cargo hold along a constant height of 1.5 m. Results from a first experiment can be found in Fig. 16(left). As can be observed, the resulting accuracy is around 15 cm up to a distance of 11 m, while, when the target is more distant from the tracker, the error of the system is significantly larger. This is due to the resolution of the camera and the focal length of the optics. In order to increase the overall accuracy, a different camera with higher resolution and a different focal length could be used. In this particular case, however, the height of the cargo hold during the second field trial was around 12 m, which indicates that the tracking performance was good enough to localize the robot everywhere inside the hold, i.e., in accordance with the requirements.

A second experiment was carried out to evaluate the repeatability of the tracker. Eight different positions were selected on a bulkhead, and the tracker was placed at a distance of around 5 m. The target was placed randomly at the selected positions and a total of 70 measurements were taken by means of the tracker. As expected, the tracker produced eight point clusters, one for each distinct position. The center of mass and the standard deviation for each cluster is shown in Fig. 16(right). Taking into account those results, it becomes obvious that the tracking is highly repeatable. Fig. 17 shows the trajectories estimated by the tracker along two of the many runs that were performed during the trials. The area covered by the runs was around 20 m^2. The tracking unit was located at a distance of around 6 m from the bulkhead.

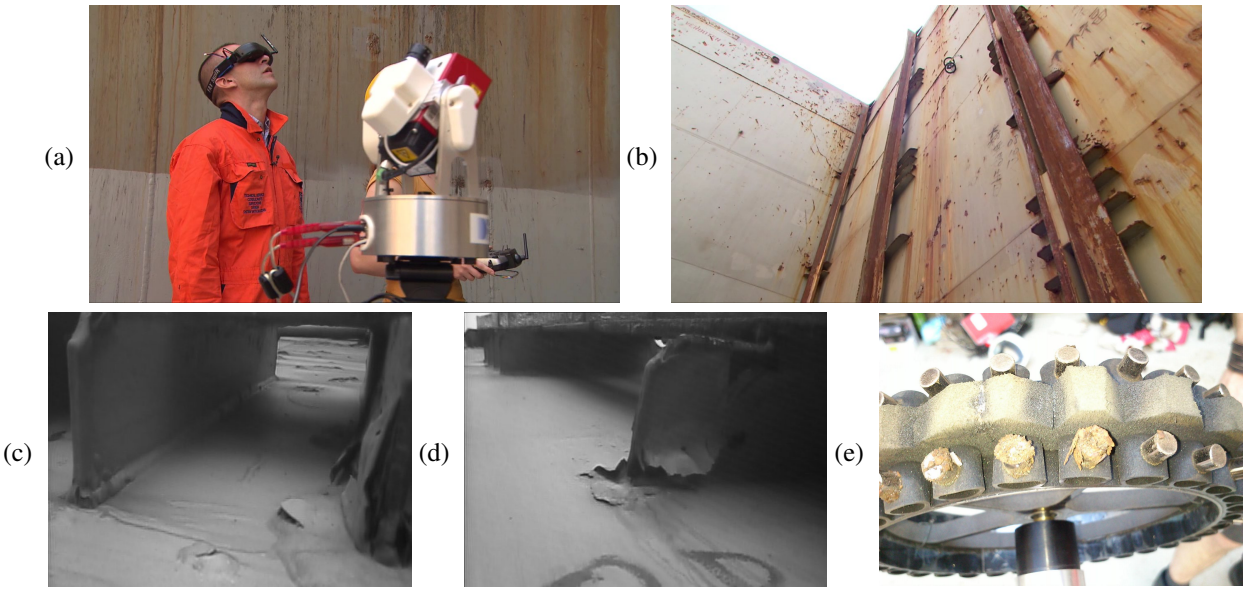

Figure 15: Second trial of the lightweight crawler: (a) experimental setup, (b) view of the wall climbed by the robot, (c–d) sample of transmitted video images from the inspection run, and (e) state of the magnets, covered in dirt and rust, after one of the runs.

6.3 Performance of the Heavyweight Inspection System

6.3.1 Heavyweight crawler

The main goal during the ship trials was to demonstrate the ability, inside a ship hold, of the MARC (1) to climb vertical walls, in general, and bulkheads, in particular, and (2) to follow vertical shell frames in autonomous mode. The ability of MARC to climb a vertical painted metallic wall inside a ship hold in a dirty environment in the presence of rust were verified in a first set of experiments. During these preliminary tests, the vehicle was positioned on the vertical walls with the support of human operators. Fig. 18(left) shows MARC climbing a bulkhead. The rope visible in the pictures is just a safety measure, i.e., it would not support the vehicle under normal working conditions. The experiments performed consisted in MARC's following a vertical stiffener frame tracked with two of the lateral laser range finders with which MARC is fitted, while climbing a bulkhead. By way of illustration, Fig. 18(right) shows the vehicle telemetry while executing one of these experiments. The different plots show, from top to bottom, the measured ranges and estimated distances, and the range and orientation errors. As expected, the vehicle manages to reduce the tracking error to zero after deliberately forcing the robot to move closer to one of the sides.

6.3.2 Thickness measurements

In order to test MARC's ability to measure thicknesses when fitted with the arm and the NDT end-effector, the crawler was made to climb a vertical bulkhead (Fig. 19(left)) while aligning itself to the stiffener frames using its lateral laser distance sensors. Once in place, the operator measuring the thickness with the ultrasound can use the robotic arm to perform the measurement. The measuring procedure starts, then, by setting a rough estimate of the desired point (x, y, z, θ) where the measure has to be taken.

Next, the arm starts to move along the previously defined vector, until contact with the surface is detected by means of reed switches or the motor's loading measure provided by the servos, which makes unnecessary any previous knowledge of the exact relative location of the surface point. Since the angle θ is provided as a rough estimate of the orientation of the surface to be measured, the actual value must then be identified. This is essential for a reliable measurement, since grinding and the UT probe placement are highly sensitive to orientation misalignment;

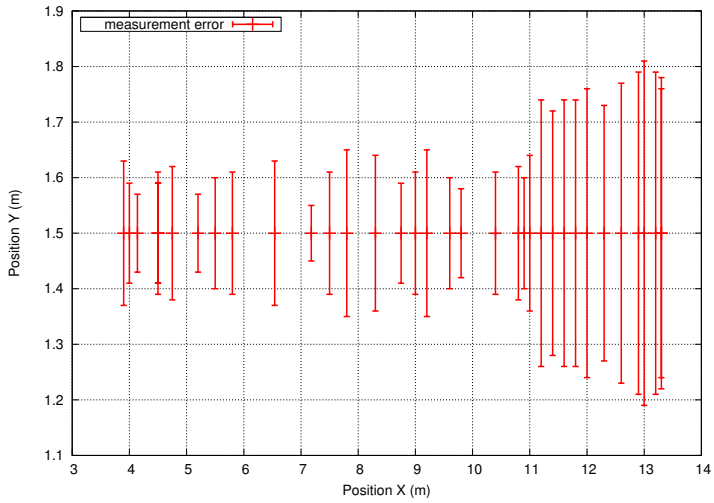

$\bar{x}$	$\bar{y}$	$\bar{z}$	dist.	σ
3.866	−3.267	−0.771	5.120	0.026
4.637	−2.039	−0.743	5.120	0.018
5.013	−0.687	−0.774	5.119	0.029
5.003	+0.732	−0.797	5.118	0.035
4.974	+0.710	+1.303	5.190	0.032
4.996	−0.690	+1.214	5.187	0.029
4.619	−2.034	+1.196	5.187	0.035
3.844	−3.251	+1.258	5.189	0.023

Figure 16: 3D tracker performance: (left) absolute positioning error as a function of distance, (right) center of mass $(\bar{x}, \bar{y}, \bar{z})$ and standard deviation (σ) for each cluster of the repeatability test [units are in meters].

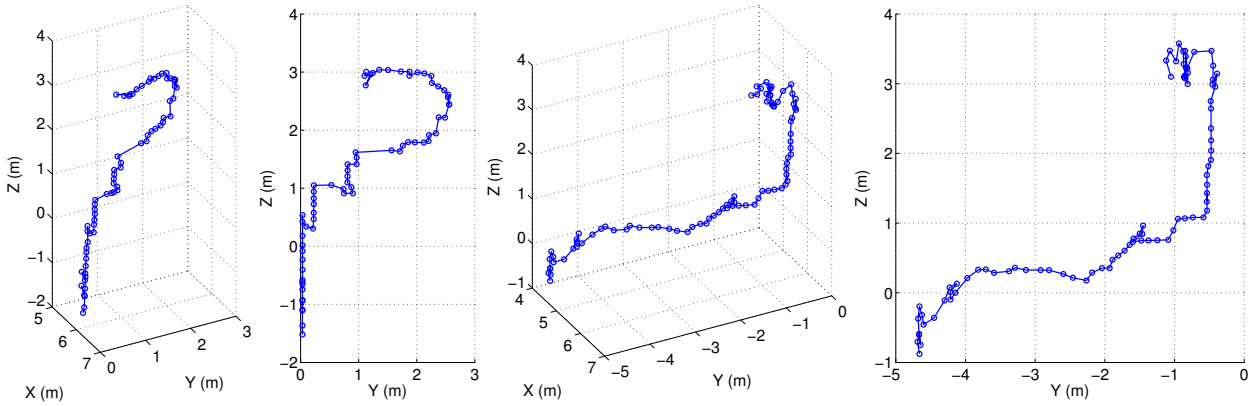

Figure 17: Two trajectories estimated by the 3D tracker: (1st,3rd) 3D perspective; (2nd,4th) YZ projection.

reed switches and the servo's angular sensors are again used to this end.

The next step starts grinding at a pre-defined load level and time duration which must be selected by the operator depending on the ship's state and amount of rust. The UT probe is next placed on the ground spot and a couplant is applied through the peristaltic pump, suitable for highly viscous fluids. Finally, the measurement is performed and a filtered A-Scan along the real UT waveform is presented to the operator. The measured waveform and its location can be stored prior to the start of a new measurement. Fig. 19(right) shows the results for one of the measurements, where the UT waveform is in red and the A-Scan is in blue. Numerous settings familiar to the UT operator, such as gain, filter bandwidth, time window, etc., can be altered at any point in time, although these settings are typically adjusted during calibration at the beginning of the survey, as required by the surveyor. The figure shows, for comparison, thickness estimates from both the peak detection algorithms and algorithms based on the auto-correlation function. The measurement, 9.1 mm, was verified by the shipyard's representative. Given the distant operation (typically above 10 m height), the number of steps to perform, and the accuracy of the operations required by the UTM, the arm's micro-controller software was designed and developed so that the measuring process was as automatic as possible, requiring minimal user intervention or knowledge of the environment.

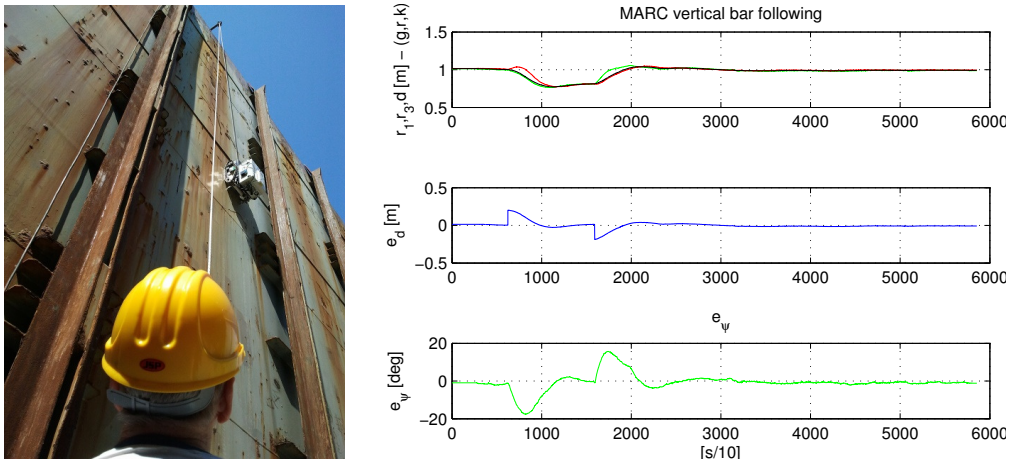

Figure 18: (left) MARC climbing a bulkhead inside the ship cargo hold. (right) MARC telemetry while following a side frame: measured ranges and estimated distance, distance error and orientation error (from top to bottom), where, in the upper plot, r1 (green) refers to the front right sensor, r3 (red) refers to the rear right sensor, and d (black) is the estimated distance to the side frame.

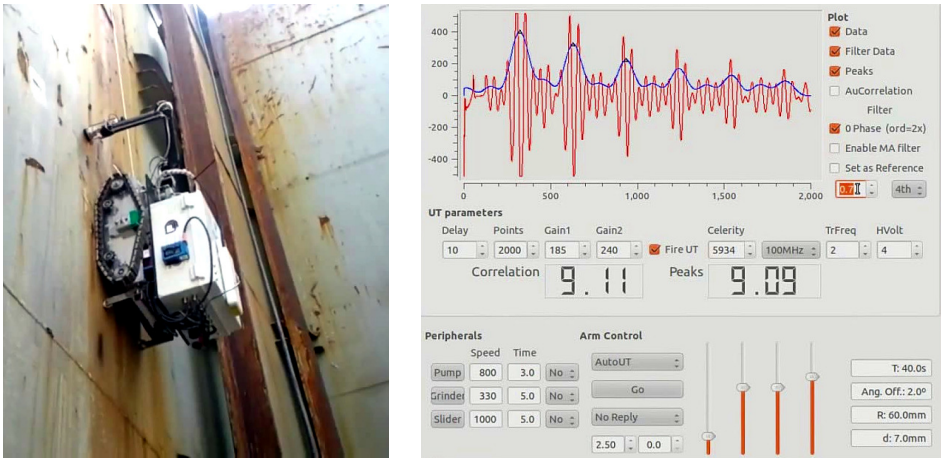

Figure 19: (left) MARC on a vertical bulkhead, taking a thickness measurement during a field trial. (right) Screenshot of the UT software.

6.4 Performance of the defect-detection solution

The performance of the defect detector has been evaluated using digital images provided by the MINOAS partners or else collected from real vessels during field trials. In general, the different images were captured without specific settings for the imaging process, particularly as to the illumination. Performance figures have been obtained for each stage of the classifier, using manually labelled images as the ground truth. Illustrative results of the defect detector are provided in Fig. 20. On the one hand, Fig. 20(a) provides results for the same input image using different energy thresholds. As can be observed, τ_E can be tuned to decrease false positives and just allow the detection of the most significant corroded areas. In the images, pixels labelled as corroded are colour-coded as red, orange, green and blue in accordance to the likelihood provided by the histogram, with red for high likelihood and blue for low likelihood. On the other hand, Fig. 20(b–c) shows the results for the full defect detector. The figure also compares the output of the crack detection stage with the output of an unguided configuration. As can be seen, the number of false positive detections is conspicuously reduced when the crack inspection makes use of the output of the corrosion detection.

Quantitative performance results for the full set of images have been obtained by calculating the percentages of false

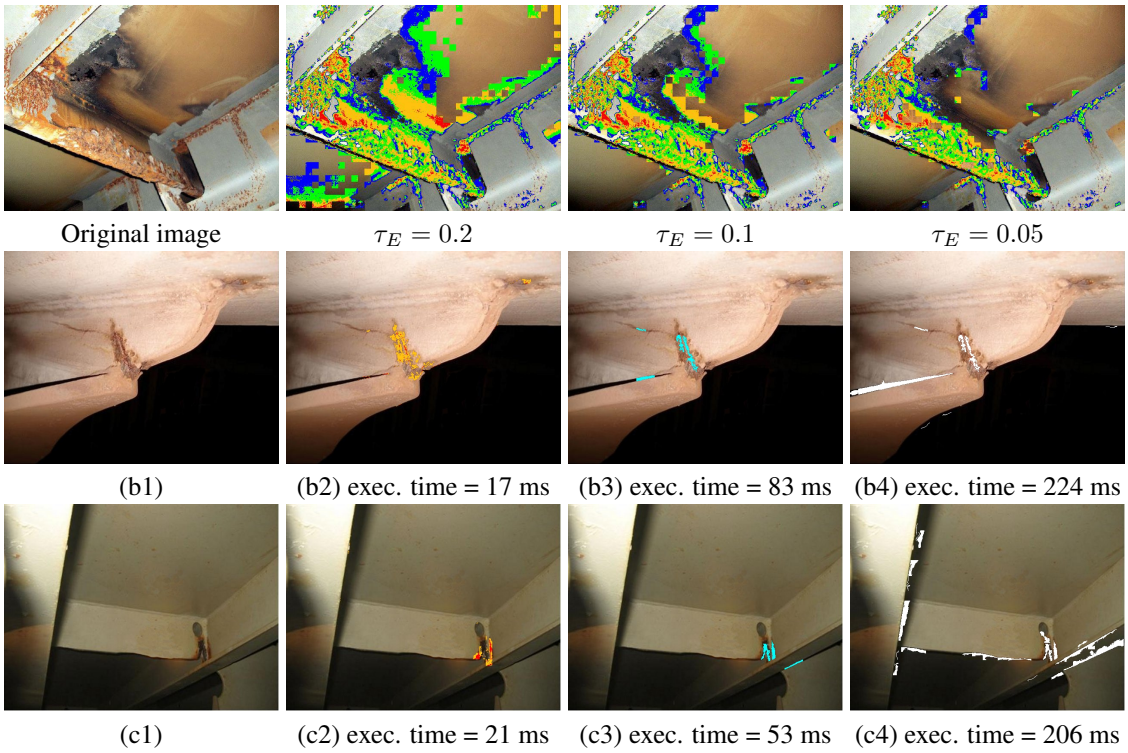

Figure 20: (a) Corroded areas detected using different energy threshold values τ_E. (b–c) Image samples and corresponding defect detections: (1) original image, (2) corrosion detector output, (3) crack detector output, and (4) crack detector output if the corrosion stage is skipped.

positives, *FP/no. pixels*, and of false negatives, *FN/no. pixels*. On the one hand, for the corrosion detector, the results are 9.80 (FP%) and 5.86 (FN%), while, for the crack detector, the results are 0.72 (FP%) and 0.57 (FN%). On the other hand, when the corrosion stage output is used to guide the crack detector, the result is a reduction in the FP% from 2.29% to 0.72%, and a speed-up in the execution time of 3.1x. This performance is in accordance with our assumption that most of the cracks in a metallic surface appear in areas which are also affected by corrosion, and prove that using corrosion to guide the crack detection results in a faster and more robust detector. Referring to the execution times, the defect detector provides corrosion-labelled images in 7–25 ms, and corrosion-guided crack-labelled images in 30–180 ms. These execution times correspond to images ranging from 120,000 to 172,000 pixels, and for a runtime environment including a laptop fitted with an Intel Core2 Duo processor (@2.20GHz, 4GB RAM).

6.5 Evaluation of the spatial content management system

The content management system was introduced during the second trial on the container ship. The tracking system was placed in a fixed position within the cargo hold. The 3D model was assigned to the topological node of the vessel as described in Section 5 and the position of the 3D tracker was calibrated by measuring several of the distances from the bulkheads. The lightweight crawler was used during the experiments. Transmitted inspection data were synchronized with the position provided by the tracking unit, thus providing information which was tagged with time and position. Live inspection views of the SCMS can be found in Fig. 21. For a start, Fig. 21(a) shows a 3D view of the hold, the position of the inspection robot, and the data blobs which had been recorded by the system. Within this view, the operator can directly select inspection data just by clicking on the corresponding blob (Fig. 21(b)). The SCMS can also show a tree view (Fig. 21(c)), where the operator can select inspection data based on the recording time, the type of data, or search for specific data contents.

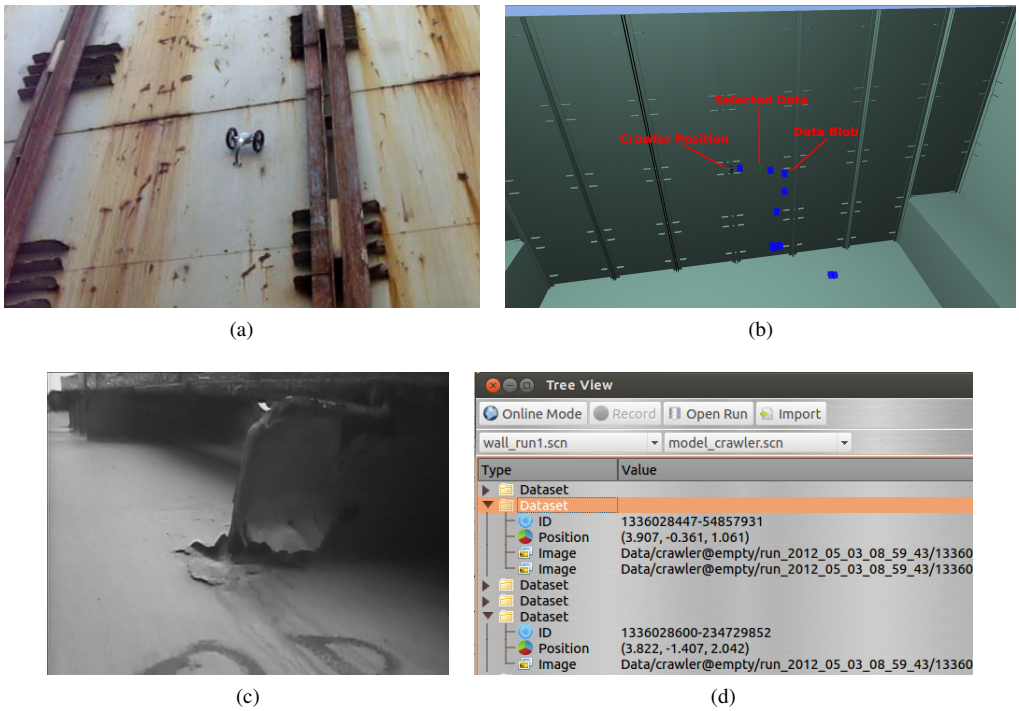

(a) (b)

(c) (d)

Figure 21: (a) Cargo hold where the SCMS evaluation took place. Illustration of SCMS operation: (b) 3D view, (c) image at the data node, and (d) tree view.

7 Conclusion and future research

This paper has introduced a vessel inspection system comprising a number of robotic systems fitted with different locomotion capabilities (aerial and magnetic crawling) and sensing modalities. Auxiliary systems, such as an integrated defect detection solution and a spatial content management system (SCMS) have been verified in field trials. The abilities of each platform have been derived directly from the requirements imposed by a re-engineered inspection procedure using robots, consisting of three distinct inspection stages. An integrated defect detection solution has been applied in order to select the critical spots for the use of non-destructive testing methods during the third stage. The areas of improvement include, apart from the industrialization of the platforms for a more robust operation, the enhancement of the locomotion capabilities together with the augmentation of the platforms' intelligence to increase its level of autonomy. The SCMS can also be enhanced by means of the semantic annotation of the structural parts, in order to lead to a more understandable representation of the inspection data, e.g., 'blistering on the upper stool between the third and fourth shell frame', as well as with the incorporation of 3D reconstruction functionality, using, e.g., laser-generated point clouds, in order to avoid any dependence on the availability of CAD models of the vessel under inspection. Finally, the collaboration between the platforms is a topic for further research.

Acknowledgments

This work was funded by the European Commission under project MINOAS (SCP8-GA-2009-233715). Francisco Bonnin-Pascual and Emilio Garcia-Fidalgo have been partially supported by the European Social Fund through, respectively, grants FPI10-43175042V and FPI11-4312 3621R (Conselleria d'Educació, Cultura i Universitats, Govern de les Illes Balears). The authors want to thank Felix Grimminger and Kristin Fondahl for their work on the hardware design of the lightweight crawler and the 3D tracking unit. Finally, the authors thank Giorgio Bruzzone, Edoardo Spirandelli, and Mauro Giacopelli for their extraordinary contribution to the design, development, and testing of the MARC platform.

References

Achtelik, M., Achtelik, M., Weiss, S., and Siegwart, R. (2011). Onboard IMU and Monocular Vision Based Control for MAVs in Unknown In- and Outdoor Environments. In *Intl. Conf. Robotics and Automation*, pages 3056–3063.

Achtelik, M., Bachrach, A., He, R., Prentice, S., and Roy, N. (2009). Autonomous Navigation and Exploration of a Quadrotor Helicopter in GPS-denied Indoor Environments. In *Intl. Aerial Robotics Competition*, pages 582–586.

Bachrach, A., Prentice, S., He, R., and Roy, N. (2011). RANGE-Robust autonomous navigation in GPS-denied environments. *J. Field Robotics*, 28(5):644–666.

Bibuli, M., Bruzzone, G., Bruzzone, G., Caccia, M., Giacopelli, M., Petitti, A., and Spirandelli, E. (2012). MARC: Magnetic Autonomous Robotic Crawler Development and Exploitation in the MINOAS Project. In *Intl. Conf. Comp. and IT Appl. in the Maritime Industries*, pages 62–75.

Bonnin-Pascual, F. (2010). Detection of cracks and corrosion for automated vessels visual inspection. Master's thesis, University of Balearic Islands. Available at http://srv.uib.es/ref/1233.html.

Bonnin-Pascual, F., Garcia-Fidalgo, E., and Ortiz, A. (2012). Semi-Autonomous Visual Inspection of Vessels Assisted by an Unmanned Micro Aerial Vehicle. In *Intl. Conf. Intell. Robots and Systems*, pages 3955–3961.

Bouabdallah, S., Murrieri, P., and Siegwart, R. (2005). Towards Autonomous Indoor Micro VTOL. *Autonomous Robots*, 18:171–183.

Bruzzone, G., Caccia, M., Bertone, A., and Ravera, G. (2009). Standard Linux for embedded real-time robotics and manufacturing control systems. *Rob. and Comp.-Integr. Manufacturing*, 25(1):178–190.

Caccia, M., Bibuli, M., and Bruzzone, G. (2010a). Definition of navigational patterns. Technical report, CNR ISSIA, Genoa, Italy.

Caccia, M., Robino, R., Bateman, W., Eich, M., Ortiz, A., Drikos, L., Todorova, A., Gaviotis, I., Spadoni, F., and Apostolopoulou, V. (2010b). MINOAS a marine inspection robotic assistant: System requirements and design. In *Symp. Intell. Autonomous Vehicles*, pages 479–484.

Chowdhary, G., Johnson, E., Magree, D., Wu, A., and Shein, A. (2013). GPS-denied Indoor and Outdoor Monocular Vision Aided Navigation and Control of Unmanned Aircraft. *J. Field Robotics*, 30(3):415–438.

Dryanovski, I., Valenti, R. G., and Xiao, J. (2013). An open-source navigation system for micro aerial vehicles. *Autonomous Robots*, 34(3):177–188.

Eich, M. and Vögele, T. (2011). Design and control of a lightweight magnetic climbing robot for vessel inspection. In *Mediterranean Conf. Control and Automation*, pages 1200–1205.

Fletcher, J. and Kattan, R. (2009). A ballast tank coating inspection data management system. http://www-.elcoship.com/papers.htm.

Fraundorfer, F., Heng, L., Honegger, D., Lee, G. H., Meier, L., Tanskanen, P., and Pollefeys, M. (2012). Vision-Based Autonomous Mapping and Exploration Using a Quadrotor MAV. In *Intl. Conf. Intell. Robots and Systems*, pages 4557–4564.

Grzonka, S., Grisetti, G., and Burgard, W. (2012). A Fully Autonomous Indoor Quadrotor. *Trans. Robotics*, 28(1):90–100.

Gurdan, D., Stumpf, J., Achtelik, M., Doth, K.-M., Hirzinger, G., and Rus, D. (2007). Energy-efficient autonomous four-rotor flying robot controlled at 1 kHz. In *Intl. Conf. Robotics and Automation*, pages 361–366.

Haralick, R. and Shapiro, L. (1992). *Computer and Robot Vision*. Addison-Wesley.

Isard, M. and Blake, A. (1998). CONDENSATION—Conditional density propagation for visual tracking. *Intl. J. Computer Vision*, 29:5–28.

Jetstream (2013). Jetstream Magnetic Crawler M250. http://www.jetstreameurope.co.uk/products/magnetic-crawler.html.

Jung, M., Schmidt, D., and Berns, K. (2010). Behavior-based obstacle detection and avoidance system for the omni-directional wall-climbing robot CROMSCI. In Fujimoto, H. et al., editor, *Emerging Trends in Mobile Robotics*, pages 73–80. World Scientific.

Kaess, M., Johannsson, H., Englot, B., Hover, F., and Leonard, J. (2010). Towards autonomous ship hull inspection using the Bluefin HAUV. In *Intl. Symp. on Techn. and the Mine Problem*.

Kalra, L., Guf, J., and Meng, M. (2006). A Wall Climbing Robot for Oil Tank Inspection. In *Intl. Conf. Robotics and Biomimetics*, pages 1523–1528.

Kim, H., Seo, K., Lee, K., and Kim, J. (2010). Development of a Multi-Body Wall Climbing Robot With Tracked Wheel Mechanism. In Fujimoto, H. et al., editor, *Emerging Trends in Mobile Robotics*, pages 439–446. World Scientific.

Koveos, Y., Kolyvas, T., and Drikos, L. (2012). Robotic Arm Development for Ultrasonic Inspection. In *Intl. Conf. Comp. and IT Appl. in the Maritime Industries*, pages 258–268.

Matsue, A., Hirosue, W., Tokutake, H., Sunada, S., and Ohkura, A. (2005). Navigation of Small and Lightweight Helicopter. *Trans. Japan Soc. for Aeronautical and Space Sciences*, 48(161):177–179.

Meier, L., Tanskanen, P., Heng, L., Lee, G. H., Fraundorfer, F., and Pollefeys, M. (2012). PIXHAWK: A micro aerial vehicle design for autonomous flight using onboard computer vision. *Autonomous Robots*, 33(1–2):21–39.

Miko (2013). Steel-Climber. http://www.miko.no/steel-climber/.

Ortiz, A., Bonnin, F., Gibbins, A., Apostolopoulou, P., Bateman, W., Eich, M., Spadoni, F., Caccia, M., and Drikos, L. (2010). First steps towards a roboticized visual inspection system for vessels. In *Intl. Conf. Emerging Technologies and Factory Automation*.

Ortiz, F., Pastor, J. A., Alvarez, B., Iborra, A., Ortega, N., Rodriguez, D., and Conesa, C. (2007). Robots for hull ship cleaning. In *Intl. Symp. on Ind. Electronics*, pages 2077–2082.

Raut, S., Patwardhan, A., and Henry, R. (2010). Design and Construction of Glossy Surface Climbing Biped Robot. In Fujimoto, H. et al., editor, *Emerging Trends in Mobile Robotics*, pages 423–430. World Scientific.

Roberts, J. F., Stirling, T., Zufferey, J.-C., and Floreano, D. (2007). Quadrotor Using Minimal Sensing For Autonomous Indoor Flight. In *European Conf. Computer Vision*.

Shang, J., Bridge, B., Sattar, T., Mondal, S., and Brenner, A. (2008). Development of a climbing robot for inspection of long weld lines. *Ind. Robot: An Intl. Journal*, 35(3):217–223.

Silva, M. F. and Tenreiro, J. (2010). *A Survey of Technologies and Applications for Climbing Robots Locomotion and Adhesion*, Climbing and Walking Robots, Behnam M. (Ed.), chapter 1, pages 1–22. InTech.

Tâche, F., Fischer, W., Caprari, G., Siegwart, R., Moser, R., and Mondada, F. (2009). Magnebike: A magnetic wheeled robot with high mobility for inspecting complex-shaped structures. *J. Field Robotics*, 26(5):453–476.

Tanneberger, K. and Grasso, A. (2011). MINOAS Deliverable (D1): Definition of the Inspection Plan / Definition of Acceptance Criteria. http://minoasproject.eu/excibition/Publications/PDF/D1.pdf.

Thrun, S., Fox, D., Burgard, W., and Dellaert, F. (2000). Robust Monte Carlo Localization for Mobile Robots. *Artificial Intelligence*, 128(1–2):99–141.

Wenzel, K. E., Masselli, A., and Zell, A. (2011). Automatic Take Off, Tracking and Landing of a Miniature UAV on a Moving Carrier Vehicle. *J. Intel. Robotic Systems*, 61(1–4):221–238.

Yamaguchi, T. and Hashimoto, S. (2010). Fast crack detection method for large-size concrete surface images using percolation-based image processing. *Machine Vision and Applications*, 21(5):797–809.

Zingg, S., Scaramuzza, D., Weiss, S., and Siegwart, R. (2010). MAV Navigation through Indoor Corridors Using Optical Flow. In *Intl. Conf. Robotics and Automation*.